Available online at www.sciencedirect.com
SCIENCE DIRECT®
Journal of Sound and Vibration 278 (2004) 233–256
JOURNAL OF SOUND AND VIBRATION
www.elsevier.com/locate/jsvi

Dynamic analysis of modal shifting and mode jumping in thermally buckled plates

H. Chen, L.N. Virgin*

Department of Mechanical Engineering, Pratt School of Engineering, Duke University, Durham, NC 27708-0300, USA

Received 20 June 2003; accepted 3 October 2003

Abstract

Both analytical and finite element investigations are performed for the various static and dynamic aspects of the mode jumping phenomenon of a simply-supported rectangular plate heated deeply into the post-buckling regime. For the analytical method, the von Kármán plate equation is reduced to a system of non-linear ODEs by expressing the transverse deflection as a series of linear buckling modes. The ODEs, combined with the non-linear algebraic constraint equations obtained from in-plane boundary conditions, are then solved numerically under the parametric variation of the temperature. The results are checked by the finite element method, where a hybrid static–dynamic scheme is implemented. The contribution of each assumed (buckling) mode component is studied systematically. Characterized by the strong geometrical non-linearity, the secondary bifurcation point of the thermally loaded plate with fixed in-plane boundary conditions occurs far beyond the primary buckling point, and the jump behavior cannot be predicted correctly without sufficient assumed modes. Stationary bifurcation analysis indicates that while the post-buckling deflection before mode jumping is composed of pure symmetric modes, additional pure antisymmetric modes will appear after the occurrence of the snapping and they play the role of destabilizing the equilibrium. Furthermore, by monitoring natural frequencies and modal shapes, we find that a mode shifting phenomenon (the exchanging of vibration modes) exists in the primary post-buckling regime. Breaking of the symmetry of the dynamic modes is also found. By introducing a linear temperature sweeping scheme, transient analysis is performed to capture the snapping phenomenon dynamically, which occurs with moderate heating ratio. Comparison between the analytic and finite element results shows good agreement.

*Corresponding author. Tel.: +1-919-660-5342; fax: +1-919-660-8963.
E-mail address: l.virgin@duke.edu (L.N. Virgin).

0022-460X/$ - see front matter © 2003 Elsevier Ltd. All rights reserved.
doi:10.1016/j.jsv.2003.10.054

1. Introduction

One of the most interesting aspects of the post-buckled equilibrium behavior of flat plates and panels is that they may exhibit finite jumps in their buckled modes when subject to high levels of compressive axial load. This form of secondary bifurcation, or mode jumping, is associated with subtle interplay between modes and has received considerable attention in Refs. [1–20].

After Stein's initial observation of such transient change in the post-buckled deformation states in a compression test of a multi-bay, flat aluminum plate [1], numerous analytical studies of the snap phenomenon and related issues have been performed on compressively loaded plates [2–9]. Linear eigenvalue analysis (see, for example, Refs. [3,4,21]) indicates there exist many compound bifurcation points in the plots of critical loads versus the aspect ratio for various boundary conditions. Thus, it seems reasonable to assume that such critical loads are generated by a splitting process of the compound points by the variation of the aspect ratio from a particular value giving the multiple eigenvalues, and that the jump of the post-buckled modes caused by the secondary instability of the equilibrium can be explained by coupling effects between the competitive modes [6].

Many of the previous efforts exploring the post-buckling behavior and snap phenomena of axially compressed plates are carried out by using modal approximations, with the transverse deflection represented by a series of linear buckling modes [2–9,13,22–24]. However, as pointed out by Stoll [9], analyses using only two-term representations of the transverse displacements have failed to predict the snap phenomena of simply-supported plates [5,8,15]. With additional terms incorporated, or by using different approaches, the secondary instability is predicted [3,4,6,9,21]. The failure of the prediction of the secondary buckling may be attributed to the "contamination" of active co-ordinates—the assumed modes—by the passives—usually the higher modes for square plates [25].

The expansion of results obtained from a particular aspect ratio to a range of lengths has been achieved by Nakamura and Uetani [6] and Everall and Hunt [3,4,21,25]. Nakamura and Uetani systematically identified the consistent set of transverse deformation terms which is required to accurately predict the mode jumping for simply-supported plates over a range of lengths. Alternatively, Everall and Hunt comparatively studied the mode jumping in the buckling of struts and plates for a particular set of boundary conditions and presented their results by using the parametric space of Arnol'd tongues.

Although a good deal of qualitative insight can be gained using approximate analytical techniques, finite element analysis is well suited to study this more complex behavior [10–12,14,26,27]. Since it is difficult to use the static path-following method to locate the disconnected stable equilibriums before and after the jump, different schemes are used to find the stable equilibrium path after the jump. One scheme is to guess a solution which is away from the primary post-buckling equilibrium as the starting computational point for the jumped branch. After the convergence of this trial solution is achieved, a standard path-following method is continued to find the jumped path [14,27]. Another is the well-known hybrid static–dynamic computational approach which is developed and used by Riks et al. [10] to model one bay of Stein's aluminum plate. It has been used widely to solve various problems, for example, the damage of a compressed sandwich panel [11] and the mode jumping of the thermally loaded plate [26].

To broaden the investigation of mode jumping from the static approach to dynamics and from mechanical loading situations to those of thermal loading, in this paper, we use both finite element and analytical approaches to study a thermally loaded simply-supported plate with fixed in-plane boundary conditions. Unlike its mechanically-loaded counterpart, this kind of thermally loaded plate demonstrates strong geometric non-linearity, which is generated by the coupling between the flexural and in-plane deformations. Linear analysis shows that there is no compound point in the plot describing the critical load versus aspect ratio. Moreover, the secondary bifurcation occurs far beyond the primary buckling point, e.g., the secondary buckling load is about 46 times that of the critical buckling load for a particular aspect ratio. Therefore, it is no surprise that the jumping behavior cannot be predicted correctly without sufficient assumed modes. A hybrid static–dynamic finite element strategy is used for transition between the static and dynamic analyses, while for the analytical approach—by assuming a series of linear buckling modes for the transverse deflections—the governing partial differential equations (PDEs) are reduced to a series of amplitude equations (ODEs) with the Galerkin procedure. The numerical continuation package AUTO [28] is then used to track the solution path and log the bifurcation points for these ODEs. The amplitude contributions from each mode to the post-primary and post-secondary equilibrium states are studied systematically. Natural frequencies and vibration mode shapes are monitored, as well as the equilibrium path toward the secondary buckling. The dynamic character of the snap is captured by the transient (or non-stationary) analysis in which a linear sweep scheme is implemented. The hysteretic behavior, which is best represented by the load versus displacement relationship, is obtained by first increasing the temperature beyond the secondary bifurcation point, then decreasing it so that the plate jumps back to its original configuration. Comparison between the analytical and finite element results shows good agreement.

2. Analytical method

2.1. Partial differential equations

Consider a thermally loaded isotropic rectangular plate with uniform thickness h and edge dimensions a and b, shown in Fig. 1, in which the xy plane coincides with the midplane. Three

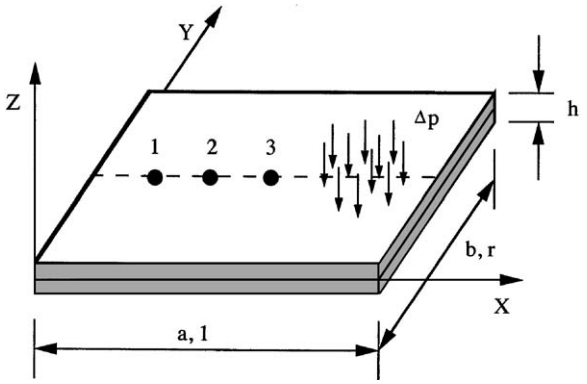

Fig. 1. Schematic of the plate.

representative nodes (1,2,3) located on the central line with respect to the plate width are monitored for deflection and dynamic response. The components of the displacement at a point, occurring in the x, y, z directions, are denoted by $u(x, y, t)$, $v(x, y, t)$, and $w(x, y, t)$, respectively. In the following analysis, a small out-of-plane initial imperfection $w_0(x, y)$ is also taken into account.

The dynamic behavior of a thin post-buckled plate with initial imperfection is described by the von Kármán large displacement equation and the associated compatibility equation [16,22,29], which can be written

$$D\nabla^4(w - w_0) + m\frac{\partial^2 w}{\partial t^2} + C\frac{\partial w}{\partial t} + \Delta p = F_{yy}w_{xx} + F_{xx}w_{yy} - 2F_{xy}w_{xy}, \tag{1}$$

$$\nabla^4 F = Eh((w_{xy})^2 - (w_{0xy})^2 - w_{xx}w_{yy} + w_{0xx}w_{0yy}), \tag{2}$$

where subscripts denote partial differentiation with respect to the variable, for example, $(\,)_{xx} = \partial^2(\,)/\partial x^2$, $D = Eh^3/12(1 - \nu^2)$ is the flexural rigidity, m is the mass density per unit area, C is the viscous damping, Δp is the vertical loading per unit area, E is Young's modulus, ν is the Poisson ratio, and F is the Airy stress function, defined by

$$N_x = \frac{\partial^2 F}{\partial y^2}, \quad N_y = \frac{\partial^2 F}{\partial x^2}, \quad N_{xy} = -\frac{\partial^2 F}{\partial x \partial y}, \tag{3}$$

where N_x, etc., indicate the in-plane stress resultants.

Membrane forces N_x and N_y can be further considered to be composed of two parts: the uniformly distributed forces (P_x and P_y) and the variational ones (F^p_{yy} and F^p_{xx}). Their relationship can be described by the following expressions:

$$N_x = P_x + F^p_{yy}, \quad N_y = P_y + F^p_{xx}. \tag{4, 5}$$

It will be seen later that this kind of partition of the membrane forces is consistent with that of the Airy stress function obtained by solving the compatibility equation (2), regardless of what specific out-of-plane boundary conditions are applied on the edges.

Introducing dimensionless quantities indicated by a tilde,

$$\begin{aligned}
&x = a\tilde{x}, \quad y = a\tilde{y}, \quad w = \sqrt{\frac{D}{Eh}}\,\tilde{w}, \quad F = D\tilde{F},\\
&N_x = \frac{D}{a^2}\tilde{N}_x, \quad N_y = \frac{D}{a^2}\tilde{N}_y, \quad N_{xy} = \frac{D}{a^2}\tilde{N}_{xy}, \quad m = \frac{D}{a^4}\tilde{m},\\
&C = \frac{\sqrt{Dm}}{a^2}\tilde{C}, \quad \Delta p = \frac{D}{a^4}\sqrt{\frac{D}{Eh}}\,\delta p, \quad u = \frac{D}{Eha}\tilde{u}, \quad v = \frac{D}{Eha}\tilde{v},\\
&t = \sqrt{\frac{a^4 m}{D}}\,\tau, \quad r = \frac{b}{a}\ \text{(aspect ratio)},
\end{aligned} \tag{6}$$

enables Eqs. (1)–(3) to be simplified as

$$\tilde{\nabla}^4(\tilde{w} - \tilde{w}_0) + \tilde{w}'' + \tilde{C}\tilde{w}' + \delta p = \tilde{F}_{\tilde{y}\tilde{y}}\tilde{w}_{\tilde{x}\tilde{x}} + \tilde{F}_{\tilde{x}\tilde{x}}\tilde{w}_{\tilde{y}\tilde{y}} - 2\tilde{F}_{\tilde{x}\tilde{y}}\tilde{w}_{\tilde{x}\tilde{y}}, \tag{7}$$

$$\tilde{\nabla}^4\tilde{F} = \tilde{w}^2_{\tilde{x}\tilde{y}} - \tilde{w}^2_{0\tilde{x}\tilde{y}} - \tilde{w}_{\tilde{x}\tilde{x}}\tilde{w}_{\tilde{y}\tilde{y}} + \tilde{w}_{0\tilde{x}\tilde{x}}\tilde{w}_{0\tilde{y}\tilde{y}}, \tag{8}$$

$$\tilde{N}_{\tilde{x}} = \tilde{F}_{\tilde{y}\tilde{y}}, \quad \tilde{N}_{\tilde{y}} = \tilde{F}_{\tilde{x}\tilde{x}}, \quad \tilde{N}_{\tilde{x}\tilde{y}} = -\tilde{F}_{\tilde{x}\tilde{y}}, \tag{9}$$

where the primes denote differentiation with respect to τ, the non-dimensional time, and the non-dimensional bi-harmonic operator is defined as

$$\tilde{\nabla}^4(\,) = \frac{\partial^4(\,)}{\partial\tilde{x}^4} + 2\frac{\partial^4(\,)}{\partial\tilde{x}^2\partial\tilde{y}^2} + \frac{\partial^4(\,)}{\partial\tilde{y}^4}.$$

For simplicity, in the remainder of the paper we use the non-dimensional values and drop the tilde.

2.2. Boundary conditions

For a plate with unit length and width r, all edges are assumed to be simply supported but clamped in plane, i.e., longitudinal and lateral edges are prevented from moving in the x or y directions, respectively. Thus, the boundary conditions can be written as

$$\begin{aligned} &w = w_{xx} = 0, \quad N_{xy} = 0, \quad u = 0 \quad \text{at } x = 0, 1, \\ &w = w_{yy} = 0, \quad N_{xy} = 0, \quad v = 0 \quad \text{at } y = 0, r. \end{aligned} \tag{10}$$

Out-of-plane boundary conditions are satisfied by expanding the flexural deflection with a series of linear buckled modes which satisfy the boundary constraints automatically. In-plane boundary conditions given in Eq. (10), however, cannot be implemented directly by an analytical approach, in which constraint equations are usually expressed by the in-plane displacement variables and edge forces. This makes it more difficult to solve a thermally loaded problem than to obtain solutions in a mechanical loading situation because in the former case even the uniformly distributed forces P_x and P_y cannot be given explicitly. Therefore, it is necessary to find the implicit relationship between those in-plane displacements and edge forces.

For a plate with all edges fixed in plane, we need constraint equations to prevent edges from moving. This is achieved by introducing the following zero end-shortening conditions and from which P_x and P_y can be determined:

$$\int_0^1 \frac{\partial u}{\partial x}\,\mathrm{d}x = 0, \quad \int_0^r \frac{\partial v}{\partial y}\,\mathrm{d}y = 0. \tag{11}$$

The above two integral conditions should be satisfied across the width and along the length, respectively. It will be shown later that for a simply-supported plate with transverse deflection w expanded in double sine waves, these zero end-shortening conditions are satisfied exactly, not in an average sense as indicated in some previous papers [3,7]. By considering the strain-displacement and stress–strain relationships, the above equations are transformed to

$$\begin{aligned} P_x - \nu P_y &= \delta T + \int_0^1 \left[F^p_{yy} - \nu F^p_{xx} - \frac{1}{2}\left(\frac{\partial w}{\partial x}\right)^2 + \frac{1}{2}\left(\frac{\partial w_0}{\partial x}\right)^2 \right] \mathrm{d}x, \\ P_y - \nu P_x &= \delta T + \frac{1}{r}\int_0^r \left[F^p_{xx} - \nu F^p_{yy} - \frac{1}{2}\left(\frac{\partial w}{\partial y}\right)^2 + \frac{1}{2}\left(\frac{\partial w_0}{\partial y}\right)^2 \right] \mathrm{d}y, \end{aligned} \tag{12}$$

where

$$\delta T = \frac{Eha^2}{D}\alpha\Delta T \tag{13}$$

is the non-dimensional temperature change.

The uniformly distributed in-plane stress resultants P_x and P_y are then obtained as

$$P_x = \frac{\bar{P} + v\bar{Q}}{1-v^2} + \frac{\delta T}{1-v}, \quad P_y = \frac{\bar{Q} + v\bar{P}}{1-v^2} + \frac{\delta T}{1-v}, \tag{14, 15}$$

where

$$\bar{P}(y) = \int_0^1 \left[F^p_{yy} - vF^p_{xx} - \frac{1}{2}\left(\frac{\partial w}{\partial x}\right)^2 + \frac{1}{2}\left(\frac{\partial w_0}{\partial x}\right)^2 \right] \mathrm{d}x, \tag{16}$$

$$\bar{Q}(x) = \frac{1}{r}\int_0^r \left[F^p_{xx} - vF^p_{yy} - \frac{1}{2}\left(\frac{\partial w}{\partial y}\right)^2 + \frac{1}{2}\left(\frac{\partial w_0}{\partial y}\right)^2 \right] \mathrm{d}y. \tag{17}$$

It is clear that before buckling, $\bar{P} = \bar{Q} = 0$ and $P_x = P_y = \delta T/(1-v)$ as expected in conventional linear buckling or small displacement analysis; however, this no longer holds when the plate is heated into the post-buckling regime since at this stage the coupling of the transverse displacement takes effect.

2.3. Transformation to ordinary differential equations

For a simply-supported plate, both the transverse deflection w and the initial imperfection w_0 may be expressed as double Fourier series:

$$w(x,y) = \sum_{k,l} A_{kl} \sin(k\pi x) \sin\left(\frac{l\pi y}{r}\right), \tag{18}$$

$$w_0(x,y) = \sum_{k,l} A_{0kl} \sin(k\pi x) \sin\left(\frac{l\pi y}{r}\right), \tag{19}$$

where A_{kl} represents the amplitude of the buckling mode with k and l half-waves over the longitudinal and lateral directions, respectively; odd values of the subscripts k and l denote the symmetrical modes while even values denote the antisymmetrical ones.

The spatial–temporal PDEs and the integral constraint equations which govern the dynamic behavior of the plate can be transformed to a system of non-linear ODEs and algebraic equations governing the modal amplitudes by expanding the former in terms of the expanded displacement forms described in Eqs. (18) and (19).

To achieve this, we first solve the compatibility equation. Just as we partition the in-plane resultants N_x and N_y into the uniformly distributed part and the variational part in Section 2.2, the general solution of Eq. (8) is assumed to consist of a homogeneous solution $F^h(x,y)$ and a particular solution $F^p(x,y)$:

$$F(x,y) = F^h(x,y) + F^p(x,y), \tag{20}$$

where the homogeneous solution takes the form

$$F^h(x,y) = \frac{y^2}{2}P_x + \frac{x^2}{2}P_y. \tag{21}$$

Substituting Eqs. (18) and (19) into Eq. (8) and carrying out some trigonometric, algebraic, and calculus operations, the particular part of the Airy's function is obtained as

$$F^p(x,y) = \sum_k \sum_l \sum_m \sum_n \left(\frac{r^2}{4}\right)(A_{kl}A_{mn} - A_{0kl}A_{0mn})\mathbf{S}_x^{\mathrm{T}}\mathbf{C}_{klmn}\mathbf{S}_y, \tag{22}$$

where

$$\mathbf{S}_x = \begin{Bmatrix} \cos(k+m)\pi x \\ \cos(k-m)\pi x \end{Bmatrix}, \quad \mathbf{C}_{klmn} = \begin{bmatrix} C_{1klmn} & C_{2klmn} \\ c_{3klmn} & C_{4klmn} \end{bmatrix}, \quad \mathbf{S}_y = \begin{Bmatrix} \left(\dfrac{\cos(l+n)\pi y}{r}\right) \\ \left(\dfrac{\cos(l-n)\pi y}{r}\right) \end{Bmatrix}. \tag{23}$$

The coefficients in matrix $\mathbf{C}_{klmn}$ are given by

$$C_{1klmn} = \frac{(klmn - k^2n^2)}{[(k+m)^2r^2 + (l+n)^2]^2}, \quad C_{2klmn} = \frac{(klmn + k^2n^2)}{[(k-m)^2r^2 + (l+n)^2]^2},$$

$$C_{3klmn} = \frac{(klmn + k^2n^2)}{[(k+m)^2r^2 + (l-n)^2]^2}, \quad C_{4klmn} = \frac{(klmn - k^2n^2)}{[(k-m)^2r^2 + (l-n)^2]^2}, \tag{24}$$

in which $C_{4klmn} = 0$ if $k = m$ and $l = n$.

Clearly, the Airy stress function $F(x,y)$ satisfies the zero shear stress boundary conditions along edges (Eq. (10)). We are now able to obtain the homogeneous solution $F^h(x,y)$ by solving the zero end-shortening conditions presented in Eq. (12), which are rewritten as

$$P_x - \nu P_y = \delta T + \bar{P}(y), \quad P_y - \nu P_x = \delta T + \bar{Q}(x), \tag{25}$$

where δT represents the non-dimensional end shortening attributed to the temperature rising, while $\bar{P}(y)$, $\bar{Q}(x)$, defined in Eqs. (16) and (17), denote the end shortening caused by the particular solution of the compatibility equation.

The two end-shortening conditions given by Eq. (12) seem too rigorous to be satisfied exactly, since this requires that for any lines with fixed y values, the shortening through the length should be the same, and the similar condition should also be satisfied for each line across the width. However, we will prove that under the assumption of the double Fourier expansion of the transverse deflection $w(x,y)$ the end-shortening components $\bar{P}(y)$ and $\bar{Q}(x)$ are indeed constant, i.e., they do not depend on x or y.

Substituting Eqs. (18), (19), and (22) into the first equation (12), after some algebraic and calculus manipulations, we obtain

$$\bar{P}(y) = -\frac{\pi^2}{8}\sum_{\substack{l,k,n \\ l\neq n}} (A_{kl}A_{kn} - A_{0kl}A_{0kn})\left[\frac{k^2(n-l)}{n+l}\cos\frac{(l+n)\pi y}{r} + \frac{k^2(n+l)}{(n-l)}\cos\frac{(l-n)\pi y}{r}\right] - \frac{\pi^2}{8}\sum_k\sum_l (A_{kl}^2 - A_{0kl}^2)k^2.$$

Taking the derivative of $\bar{P}(y)$, it is easy to verify that $\mathrm{d}\bar{P}(y)/\mathrm{d}y = 0$, therefore $\bar{P} = \text{constant}$. By the same reasoning, we get $\bar{Q} = \text{constant}$. Since both of these two shortening components are constant, their values can be easily obtained by integrating Eqs. (16) and (17) with respect to y and x, respectively:

$$\begin{aligned}\bar{P} &= \int_0^r\int_0^1 [F_{yy}^p - \nu F_{xx}^p - \tfrac{1}{2}(w_x^2 - w_{0x}^2)]\,\mathrm{d}x\,\mathrm{d}y \\ &= -\frac{\pi^2}{8}\sum_k\sum_l (A_{kl}^2 - A_{0kl}^2)k^2. \end{aligned} \tag{26}$$

Similarly,

$$\bar{Q} = -\frac{\pi^2}{8r^2}\sum_k\sum_l (A_{kl}^2 - A_{0kl}^2)l^2. \tag{27}$$

Thus, the homogeneous solution F^h can be obtained by substituting Eqs. (26) and (27) into Eqs. (14) and (21).

Finally, the non-dimensional dynamic von Kármán equation (7) can be reduced to a series of non-linear ODEs with respect to the modal amplitudes A_{kl} by using a Galerkin procedure with a weighting function of $\phi_{pq}(x,y)$. The weighting function $\phi_{pq}(x,y)$ takes the form

$$\phi_{pq}(x,y) = \sin(p\pi x)\sin\left(\frac{q\pi y}{r}\right), \tag{28}$$

and the right-hand side of von Kármán's equation $f(x,y)$ and the inner product of any two functions $[g(x,y), h(x,y)]$ are defined as

$$f(x,y) = f^h(x,y) + f^p(x,y) \stackrel{\text{def}}{=} F_{yy}w_{xx} + F_{xx}w_{yy} - 2F_{xy}w_{xy}, \tag{29}$$

$$[g(x,y), h(x,y)] \stackrel{\text{def}}{=} \int_0^1\int_0^r g(x,y)h(x,y)\,\mathrm{d}x\,\mathrm{d}y, \tag{30}$$

where $f^h(x,y)$ and $f^p(x,y)$ are components attributed to the contribution of the homogeneous and particular part of Airy's stress function, respectively.

Substituting Eqs. (18)–(21) into Eq. (7) and using Galerkin's procedure, we get

$$\begin{aligned}&\ddot{A}_{mm} + C\dot{A}_{mm} + (A_{mn} - A_{0mn})\left[m^2 + \left(\frac{n}{r}\right)^2\right]^2\pi^4 \\ &\quad = \frac{4}{r}\left\{[f^h(x,y), \phi_{mn}(x,y)] + [f^p(x,y), \phi_{mn}(x,y)] - [\delta p(x,y), \phi_{mn}(x,y)]\right\},\end{aligned} \tag{31}$$

where the dots denote differentiation with respect to the non-dimensional time, τ. In addition, the first two terms on the right-hand side represent the geometric non-linearity caused by the large deflections of the plate, while the last term denotes the contribution from the external force.

By substituting Eqs. (18)–(24) and (28) into Eq. (30) and making use of the orthogonal properties of the integration of trigonometric functions, the geometric non-linear terms in Eq. (31) can be obtained explicitly as

$$[f^h(x,y),\phi_{mn}(x,y)] = -\frac{\pi^2 r}{4} A_{mn}\left[P_x m^2 + P_y\left(\frac{n}{r}\right)^2\right]^2, \tag{32}$$

$$[f^p(x,y),\phi_{mn}(x,y)] = \frac{\pi^4}{16}\sum_i\sum_j\sum_k\sum_l\sum_m\sum_n A_{ij}(A_{kl}A_{mn} - A_{0kl}A_{0mn})\mathbf{V}_x^{\mathrm{T}}\mathbf{D}\mathbf{V}_y, \tag{33}$$

where

$$\mathbf{D} = \begin{bmatrix} c_1[(k+m)j-(l+n)i]^2 & c_1[(k+m)j+(l+n)i]^2 & c_3[(k+m)j-(l-n)i]^2 & c_3[(k+m)j+(l-n)i]^2 \\ c_1[(k+m)j+(l+n)i]^2 & c_1[(k+m)j-(l+n)i]^2 & c_3[(k+m)j+(l-n)i]^2 & c_3[(k+m)j-(l-n)i]^2 \\ c_2[(k-m)j-(l+n)i]^2 & c_2[(k-m)j+(l+n)i]^2 & c_4[(k-m)j-(l-n)i]^2 & c_4[(k-m)j+(l-n)i]^2 \\ c_2[(k-m)j+(l+n)i]^2 & c_2[(k-m)j-(l+n)i]^2 & c_4[(k-m)j+(l-n)i]^2 & c_4[(k-m)j-(l-n)i]^2 \end{bmatrix},$$

$$\mathbf{V}_x = \begin{Bmatrix} \frac{1}{2} & \text{if } p = i+k+m; \text{ else } 0 \\ \pm\frac{1}{2} & \text{if } p = \pm(i-k-m); \text{ else } 0 \\ \pm\frac{1}{2} & \text{if } p = \pm(i+k-m); \text{ else } 0 \\ \pm\frac{1}{2} & \text{if } p = \pm(i-k+m); \text{ else } 0 \end{Bmatrix}, \quad \mathbf{V}_y = \begin{Bmatrix} \frac{r}{2} & \text{if } q = j+l+n; \text{ else } 0 \\ \pm\frac{r}{2} & \text{if } q = \pm(j-l-n); \text{ else } 0 \\ \pm\frac{r}{2} & \text{if } q = \pm(j+l-n); \text{ else } 0 \\ \pm\frac{r}{2} & \text{if } q = \pm(j-l+n); \text{ else } 0 \end{Bmatrix},$$

and coefficients c_1, c_2, etc., are given in Eq. (24).

Since later in Section 3, we will simulate the transient response of the thermally loaded plate under a small perturbation generated by a vertical concentrated force, which is, for example, generated by hitting the plate with an impact hammer, the external force in Eq. (31) now takes the form $\delta p = \delta\bar{p}(\tau)\delta(x-x_0)\delta(y-y_0)$. Therefore, the third component in Eq. (31) becomes

$$\begin{aligned}[\delta p(x,y),\phi_{mn}(x,y)] &= \int_0^1\int_0^r \delta\bar{p}\,\delta(x-x_0)\delta(y-y_0)\sin(m\pi x)\sin\left(\frac{n\pi y}{r}\right)\mathrm{d}x\,\mathrm{d}y \\ &= \delta\bar{p}(\tau)\sin(m\pi x_0)\sin\left(\frac{n\pi y_0}{r}\right).\end{aligned} \tag{34}$$

3. Static and dynamic context of the behavior

In this paper, both analytical and finite element approaches are used to analyze the static and dynamic behavior of the mode-jumping phenomenon of the plate as we increase and decrease the temperature quasi-statically or slowly, i.e., with a certain rate of heating.

3.1. Static equilibrium and free vibrations

For the analytical approach, the stationary solution of the non-linear ODEs derived in Section 2.3 is calculated numerically with AUTO [28], a continuation package. With the temperature as the control parameter, AUTO will follow the equilibrium path and log the bifurcation points. By choosing different combinations of modal amplitudes A_{kl}, we can study the effect of various assumed modes on the secondary bifurcation points and the stability of the equilibrium paths.

The amplitude equations presented in Eq. (31) can be written in matrix form as

$$\ddot{\mathbf{A}} + \mathbf{C}_{\mathbf{A}}\dot{\mathbf{A}} + \mathbf{K}_{\mathbf{A}}\mathbf{A} = \mathbf{f}(\mathbf{A}, \delta T), \tag{35}$$

where vector $\mathbf{A}$ consists of amplitudes of the assumed modes, $\mathbf{C}_{\mathbf{A}}$ and $\mathbf{K}_{\mathbf{A}}$ represent the corresponding damping and stiffness matrices, and $\mathbf{f}(\mathbf{A}, \delta T)$ denotes non-linear force terms.

Natural frequencies and vibration mode shapes (expressed in assumed modal amplitudes) of the plate can then be calculated by locally linearizing the dynamic system at known equilibrium states and solving the associated eigenvalue problem. Such a procedure enables us to trace the characteristics of free vibrations of the plate as we vary the temperature quasi-statically.

For the finite element method, consider a structural system with $\mathbf{d}$, a vector of nodal degrees of freedom and subjected to the temperature variation ΔT. The governing equation of motion takes the form

$$\mathbf{M}\ddot{\mathbf{d}} + \mathbf{C}\dot{\mathbf{d}} + \mathbf{f}(\mathbf{d}, \Delta T) = \mathbf{0} \tag{36}$$

where $\mathbf{f} = \mathbf{f}^i(\mathbf{d}) + \mathbf{f}^e(\mathbf{d}, \Delta T)$, with the superscripts on function $\mathbf{f}$ indicating the non-linear internal and external loads, and subsumes the static behavior associated with the equilibrium condition

$$\mathbf{f} = \mathbf{f}^i(\mathbf{d}) + \mathbf{f}^e(\mathbf{d}, \Delta T) = \mathbf{0}. \tag{37}$$

We are especially interested in the stability of equilibrium, given by the Jacobian

$$\mathbf{K}(\mathbf{d}; \Delta T) = \frac{\partial \mathbf{f}(\mathbf{d}, \Delta T)}{\partial \mathbf{d}},$$

such that if $\mathbf{K}$ is positive definite the equilibrium is stable (in the Lyapunov sense). These stability analyses of the states on the equilibrium path are conducted to locate the unstable critical point. The procedure of free vibration analysis is similar to that of the analytical approach. All finite element analyses are performed using the ANSYS software.

3.2. Transient analysis

In this paper, we are primarily interested in the fully dynamic context of the snap phenomenon especially when the temperature passes the secondary critical point. To achieve this goal, we introduce a transient analysis approach which consists of a linear sweep in temperature of the form

$$\Delta T = \Delta T_0 + Rt, \tag{38}$$

where ΔT is the change of the temperature with respect to the ambient, and R is the rate of heating [30].

It will be shown later that the dynamic snap actually occurs when the temperature just passes its critical value and a different equilibrium path results. After that, the temperature is reduced and the temperature is followed (dynamically) downward. It is interesting to note that after an intermediate snap, the new branch finally snaps back to its original path.

For the analytical approach, the amplitude equation (35) is solved numerically by using a Runge–Kutta–Verner fifth and sixth order method. The starting temperature change, ΔT_0, is set to zero and different values of the sweeping rate R are used to study their effect on the prediction of the secondary critical point. To encourage the mode jumping, a small initial dynamic perturbation is introduced by applying a vertical concentrated impulse force, which is similar to the usual approach used in a practical experiment where an impact hammer is used. This is because without such perturbation the solution will always follow its original equilibrium path even though the secondary critical point has already been passed and the equilibrium state becomes unstable, no matter how slow the temperature rises.

For the finite element method, a hybrid static–dynamic method is used [10]. The procedure consists of a combination of the classical path-following strategy with a dynamic approach, where the first method is used to follow the quasi-static (stable) part of the branch until the temperature approaches the secondary bifurcation value, then the transient analysis is initiated and the temperature keeps rising beyond the critical value. The starting value of ΔT_0 is set near the secondary buckling temperature to expedite the computational process. Rayleigh damping of the following form is assumed:

$$\mathbf{D} = \alpha\mathbf{M} + \beta\mathbf{K}, \tag{39}$$

where α and β are the mass and stiffness scalar coefficients which can be selected by analogy to a single-degree-of-freedom oscillator. Suppose the system has a fundamental natural frequency f_n and the non-dimensional damping ratio of the plate is ζ. These proportional coefficients can be determined as

$$\alpha = 2\pi\zeta f_n, \quad \beta = \frac{\zeta}{2\pi f_n}. \tag{40}$$

4. Numerical results

4.1. Model description

The methods outlined are used to analyze the mode jumping phenomenon of an isotropic aluminum rectangular plate with all edges simply supported and fixed in plane. The plate model under analysis is shown in Fig. 1. The plate dimensions are length a of 762 mm (30 in), width b of 282.2 mm (11.1 in), and thickness t of 1.9844 mm (5/64 in). The material properties used in the analysis are: Young's modulus $E = 70$ GPa, Poisson's ratio $v = 0.33$, thermal expansion coefficient $\alpha = 23 \times 10^{-6}$, mass density $\rho = 2.7143$ kg/m^3. In the dynamic analysis, the non-dimensional damping ratio ζ is set as 0.05. The x co-ordinates for three monitoring points located on the central line of the plate are $0.25a$, $0.3a$ and $0.5a$. Note, for analytical

approach the corresponding non-dimensional monitoring points are $(0.25, r/2)$, $(0.3, r/2)$, and $(0.5, r/2)$.

Since in practical experiments a perfect geometry will not occur, all the following numerical calculations, except specifically indicated, are performed on a plate with an initial imperfection in its first buckling mode. The maximum original transverse deflection of the plate is set to 30% of the plate thickness.

Finite element results are obtained from a baseline FE model, consisting of 640 eight-node shell elements (type SHELL93 in ANSYS) with 40 elements through the length and 16 elements across the width. Higher and lower mesh densities have also been used to check the convergence of the equilibrium path and the sensitivity of the onset of the secondary bifurcation. No significant difference was found.

4.2. Quasi-static analysis

The lowest three linear buckling loads for thermally loaded perfect plates with different aspect ratios are calculated using the finite element method and the results are shown in Fig. 2. With the increase of aspect ratio, although the first buckling mode always takes the (1,1) form, the higher buckling modes may change their waveforms. For example, as $r = a/b$ passes through 1.4 the second lowest buckling modes will switch from (2,1) to (3,1); while the reaching of $r = 2.0$ indicates the switching of the third lowest mode from (2,1) to (4,1). It is interesting to note that unlike the (mechanical) axially compressed case [3,4,21,25], the lowest two load lines in Fig. 2 never cross each other, thus no compound buckling points exist

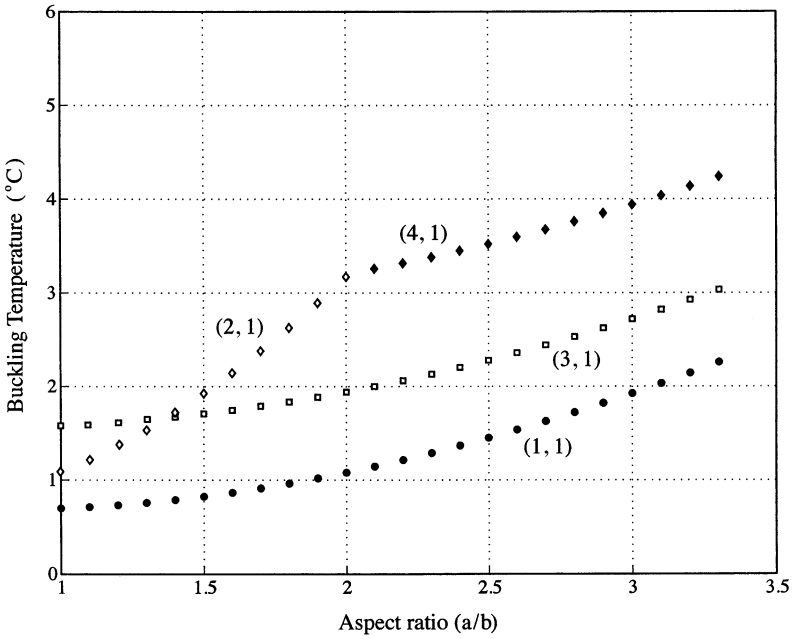

Fig. 2. Linear buckling loads for simply supported plates with various aspect ratios.

(on the lowest load line). The separation of load lines gives a hint that for a perfect plate with a particular aspect ratio the coupling effect between two primary post-buckling branches emanating from the first two critical points is not strong enough to dominate the secondary buckling behavior, and the secondary bifurcation point happens deeply in the post-buckling regime.

Let us consider a plate model described in Section 4.1, which has an aspect ratio of 0.37. In order to study the dependency of the secondary bifurcation and mode jumping on the form of assumed mode shapes, different combinations of the modal components are used and the results calculated by AUTO are listed in Table 1. For comparison purposes, finite

Table 1
Studying secondary bifurcation with various combinations of assumed modes

Assumed modes	Secondary bifurcation temperature		Secondary bifurcation type	Notes
$\{m\}$[a] $\{n\}$	Non-dimensional δT_2	Dimensional ΔT_2 (°C)		
$\{1,2,3,4,5\}$ $\{1\}$	/	/	Primary post-buckling path always stable	No mode jumping
$\{1,2,3\}$ $\{1,2\}$	1.0769×10^3	29.695	Super-critical	No mode jumping
$\{1,2,3\}$ $\{1,3\}$	/	/	Primary post-buckling path always stable	No mode jumping
$\{1,2,3,4,5\}$ $\{1,2\}$	1.6093×10^3	44.375	Super-critical	No mode jumping
$\{1,2,3,4,5\}$ $\{1,3\}$	/	/	Primary post-buckling path always stable	No mode jumping
$\{1,3,5,7,9,11\}$ $\{1,2\}$	2.2708×10^3	62.615	Sub-critical	No mode jumping
$\{1,2,3,4,5,6,7,8,9,10,11\}$ $\{1,2\}$	2.2708×10^3	62.615	Sub-critical	No mode jumping[b]
$\{1,2,3,4,5,6,7,8,9\}$ $\{1,2,3\}$	2.5139×10^3	69.312	Sub-critical	Mode jumping happens
Finite element method (path following)	2.4066×10^3	66.36	/	/

[a] m,n denotes mode shape $A_{mn}\sin(m\pi x)\sin(n\pi y/r)$.

[b] Although in this case new stable branches exist, they only occur in the range of $\delta T = 2.5836 \times 10^3 - 4.5765 \times 10^3$ or $\Delta T = 71.12$–126.19 (°C), which is beyond the secondary buckling temperature, therefore no mode jumping happens.

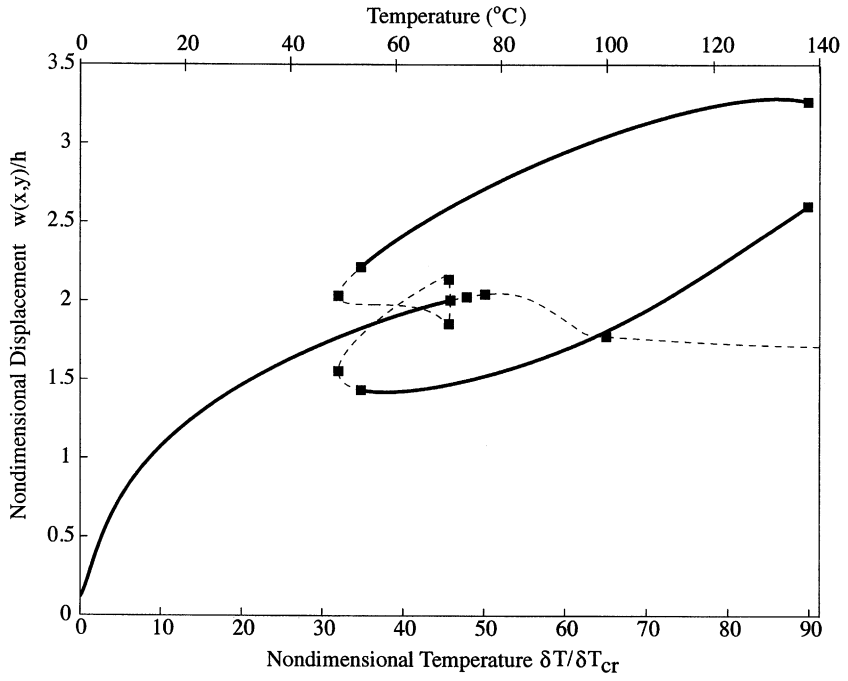

Fig. 3. Bifurcation diagram. Stable paths are shown as solid lines and unstable paths as broken lines; bifurcation points are indicated by square symbols. Deformation at $(x, y) = (1/4, r/2)$.

element results are also included. For all cases, the primary critical temperature of a perfect plate calculated by the analytical approach is $\delta T = 54.8187$ or $\Delta T = 1.5116^{\circ}\mathrm{C}$, which agrees well with the value of $\Delta T = 1.5112^{\circ}\mathrm{C}$ obtained from the finite element analysis. The secondary buckling temperature and the mode jumping behavior, however, are highly case dependent. It is easy to observe that secondary bifurcation occurs only when the assumed components contain the antisymmetric term in the y direction, i.e., $n = 2$; without such a component, the post-buckling branch is always stable. This indicates that the y direction antisymmetric modes play the role of destabilizing the primary post-buckling path. Mode jumping phenomenon can only be described correctly in the last analytical case with $\{m\} = \{1, 2, 3, \ldots, 9\}$ and $\{n\} = \{1, 2, 3\}$, where ΔT_2 is predicted as $69.31^{\circ}\mathrm{C}$, fairly close to the finite element result ($66.32^{\circ}\mathrm{C}$). Although the secondary critical temperature and bifurcation type can be obtained correctly when $w(x, y)$ contains modes with enough numbers of half-waves along the x direction but only the first two half-waves along the y direction, the jumped path cannot be predicted correctly. The above analyses suggest that if a modal approach is used, mode jumping can only be predicted correctly when enough modes are included.

In all the following analyses, we will use the modal combination of $\{m\} = \{1, 2, 3, \ldots, 9\}$ and $\{n\} = \{1, 2, 3\}$. The bifurcation diagram is shown in Fig. 3. The secondary bifurcation point occurs far from its primary buckling point, with $\delta T_2/\delta T_1 = 45.87$. This may be attributed

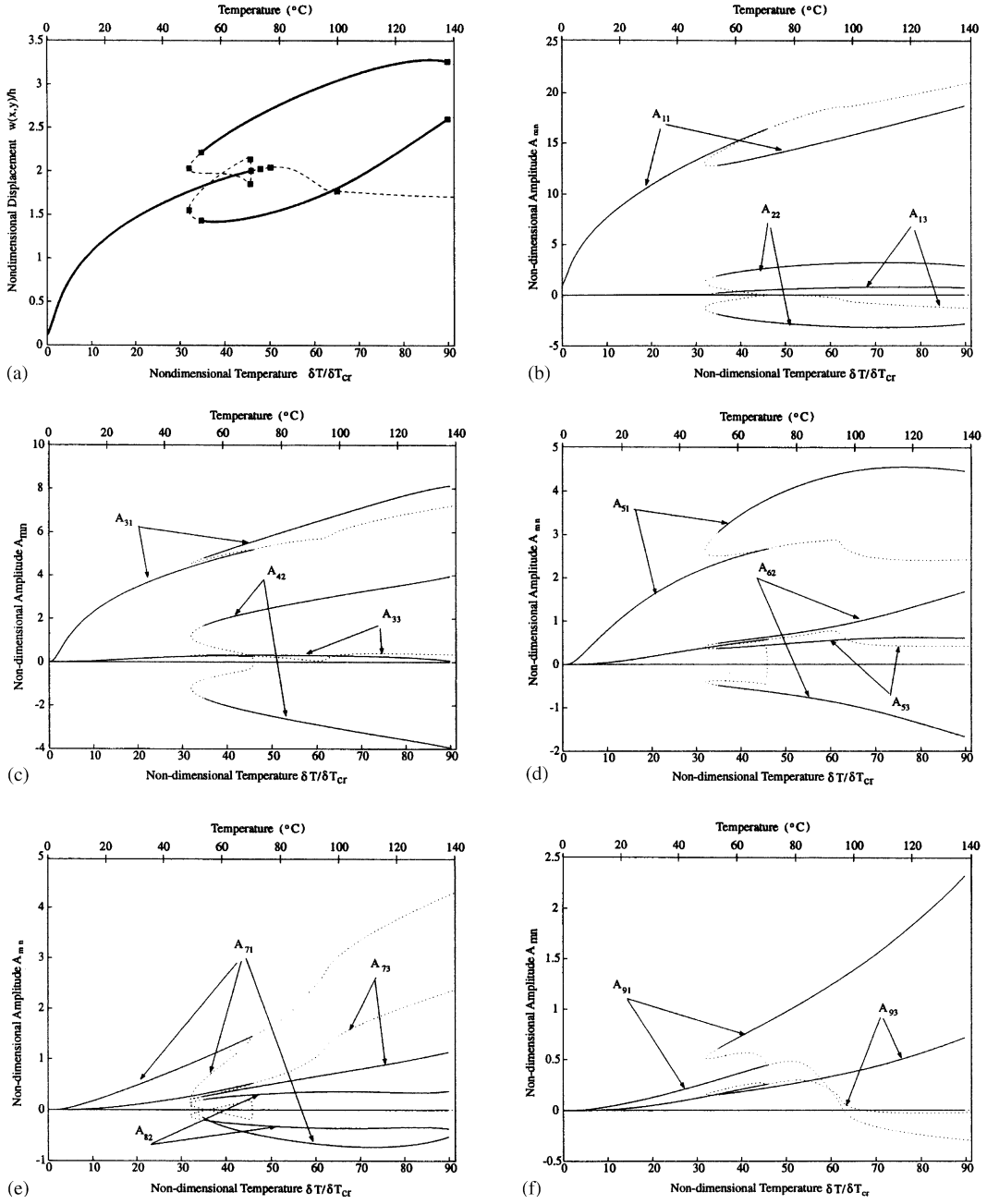

Fig. 4. Amplitude contributions: (a) bifurcation diagram; (b) A_{11}–A_{23}; (c) A_{31}–A_{43}; (d) A_{51}–A_{63}; (e) A_{71}–A_{83}; (f) A_{91}–A_{93}. Stable paths are shown as solid lines and unstable paths as broken lines.

to the strong non-linearity caused by the in-plane constraints. As the temperature increases across the secondary critical value, the primary post-buckling branch loses its stability and the plate will jump to one of the two stable equilibria. By carefully observing the diagrams of

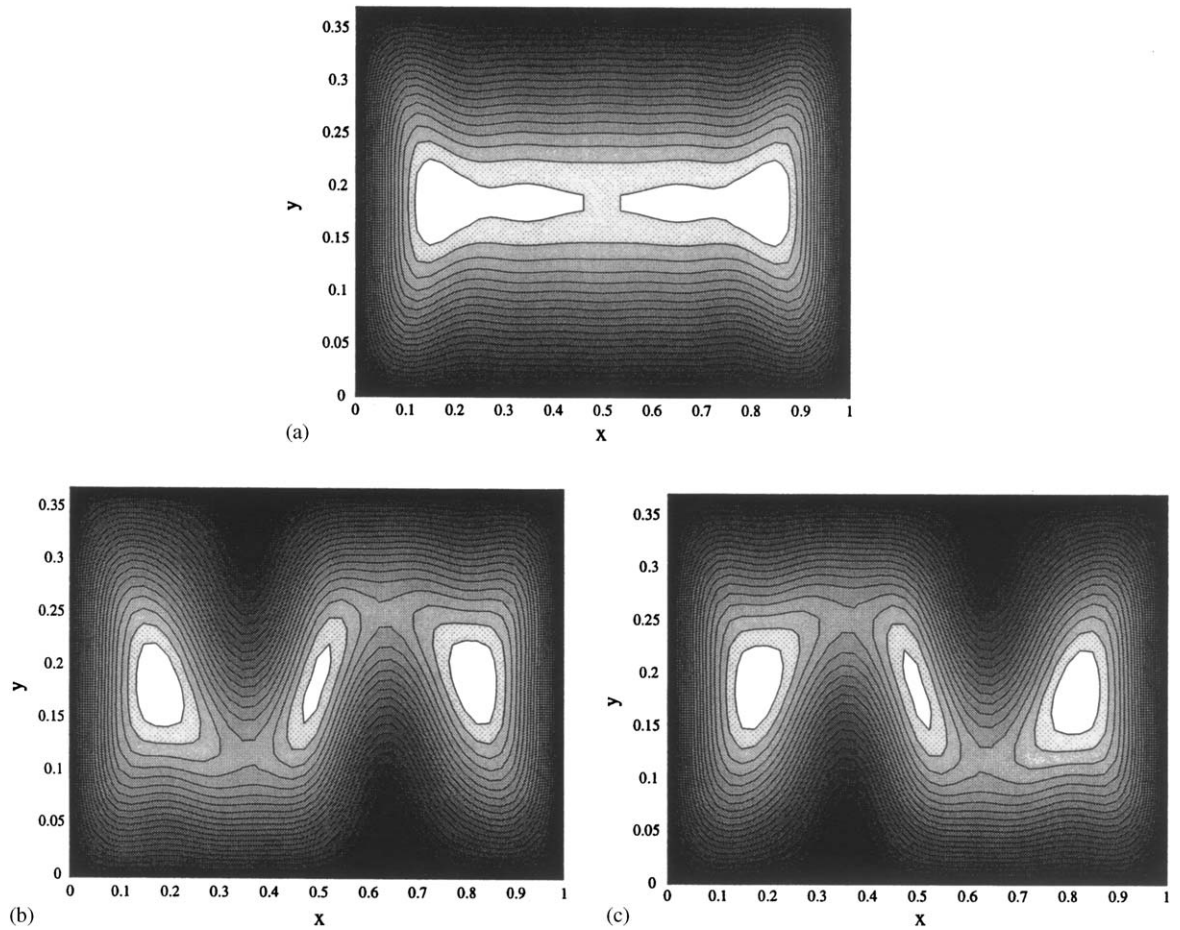

Fig. 5. Static deformation shapes at different branches: (a) at primary post-buckling path; (b) at top jumped branch; (c) at the bottom jumped branch.

amplitude contributions, shown in Fig. 4, we find that the initial post-buckling branch consists only of purely symmetric modes, e.g., A_{11}, A_{13}, A_{31}, A_{33}, A_{51}, A_{53}, A_{71}, A_{73}, A_{91} and A_{93}. The stable target branches (connected to the initial post-buckling path through unstable branches), on the other hand, contain contributions from the additional purely unsymmetrical modes, such as A_{22}, A_{42}, A_{62} and A_{82}. The mixed symmetrical modes, for example, A_{12}, A_{41}, etc., have small or no effect on capturing the snapping phenomenon in the static analysis. Therefore, it is reasonable to believe that only with at least the above 14 modes can we predict the mode jumping correctly. Additional information about static deformation shapes of the plate at $\Delta T_2 \approx 61^{\circ}\mathrm{C}$ (near the snapping point) on the primary post-buckling path and the two possible target branches are presented in Fig. 5. As expected, on the primary post-buckling branch the static deformation takes the pure symmetric form while on the two target stable branches the shape is antisymmetric with respect to the x-axis.

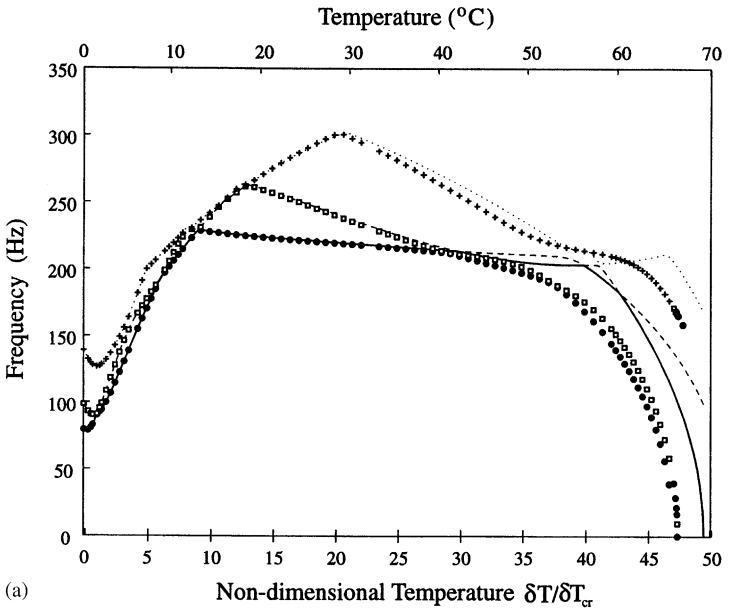

(a)

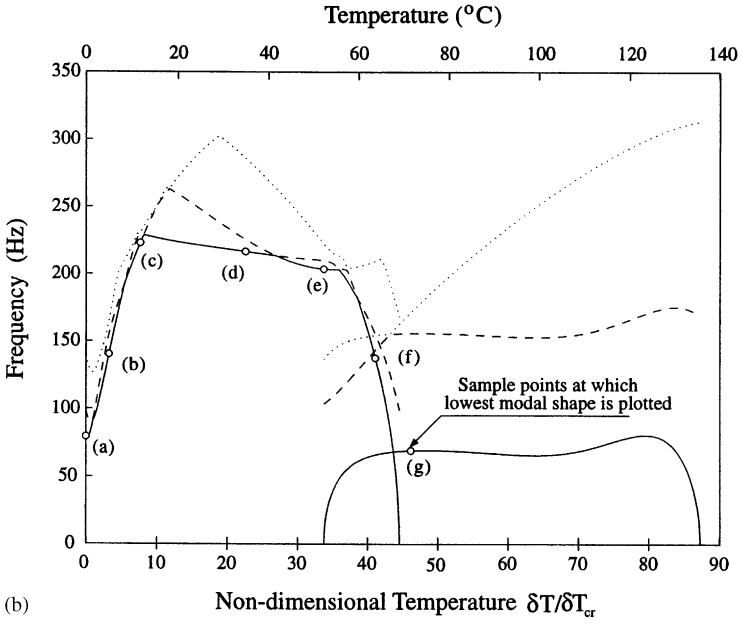

(b)

Fig. 6. Natural frequencies as a function of temperature: (a) in the range of primary post-buckling path, including FEM results (indicated by lines); (b) full range analysis. Circled symbols indicate sample points where vibration modes are plotted in Figs. 7 and 8.

4.3. *Free vibration analysis*

Natural frequencies and vibration modes are calculated as we trace the equilibrium before and after snapping. A comparison of the lowest three natural frequencies calculated by the analytical

method with those obtained by the finite element analysis is presented in Fig. 6.[1] These results agree closely in a quite wide range (up till $\delta T_2/\delta T_1 = 22$) and only when near the secondary bifurcation point, where the fundamental frequency drops to zero, do their discrepancies become obvious. The analytical result is still adequate since the relative error of the secondary critical temperatures predicted by the two methods is only 4.5%. It is worth mentioning that in the primary post-buckling regime the exchange of *vibration* modes occurs at several points, between which the fundamental mode shape remains similar but as they are passed across from the left the fundamental mode will change to a form corresponding to a previously higher frequency. We call this phenomenon the dynamic mode shifting. Similar behavior can be found in a linear analysis of an axially loaded plate [31]. However, full range non-linear analysis shows that no such exchange of modes happens after mode jumping (see Fig. 6(b)). Since the two target branches demonstrate some kind of symmetric relationship, which is verified in the static deformation plot (Fig. 5), it is no surprise to find that at the corresponding points on these branches the natural frequencies are identical.

This mode shifting phenomenon is further illustrated in Figs. 7 and 8, where the fundamental vibration mode is shown transforming from the initially $\{1,1\}$ form to $\{2,1\}$, $\{3,1\}$, $\{1,2\}$, and higher order forms. The amplitude eigenvector is normalized such that the maximum absolute value of its components is set to 1 and only those whose absolute value is greater than 0.02 are plotted. Dominant amplitude components appearing in the plots suggest that although the static analysis of mode jumping can be achieved with only the pure symmetric and pure antisymmetric assumed (static deflection) modes, the dynamic characteristics of such a phenomenon cannot be captured without the mixed mode shapes. Another interesting phenomenon is found by studying the projections of various vibration mode shapes on the xy plane. Before snapping, all projections are symmetric with respect to both the x- and y-axis and the nodal lines of the plate remain straight; after jumping, however, this neatly organized structure is broken, demonstrated by the curved nodal lines and the change of the projection form (it becomes symmetric with respect to the center of the plate).

4.4. Transient analysis

A linear sweep scheme (Eq. (38)) is used in the transient analysis of the mode jumping. To study the effect of the heating ratio qualitatively, three different values, i.e., $\Delta T/\Delta t = 100^\circ$C, 10°C and 1°C/s are used in the analytical approach and a viscous type of damping is assumed. As can be seen in Fig. 9(a), with an unrealistically fast rate of temperature change ($R = 100^\circ$C/s), the response curves follow steadily along the initial equilibrium paths even when the temperature passes through the secondary critical value, showing no evidence of mode jumping. However, the snapping phenomenon occurs in the last two cases. Further observation indicates a delay effect (overshoot) on the prediction of the snapping temperature: the snapping occurs at 71°C and 73°C for the heating rate of 1°C/s and 10°C/s, respectively, although the static analysis gives the value 69.3°C. The reasons for the existence of two oscillating ranges in the response curves for the smallest heating ratio could be explained as follows: (1) interaction between the coexisting stable solutions. For example, the first range of oscillation (from 55°C to 71°C) corresponds to the

[1] In this figure different symbols are used to identify the order of the modes rather than the specific modes themselves.

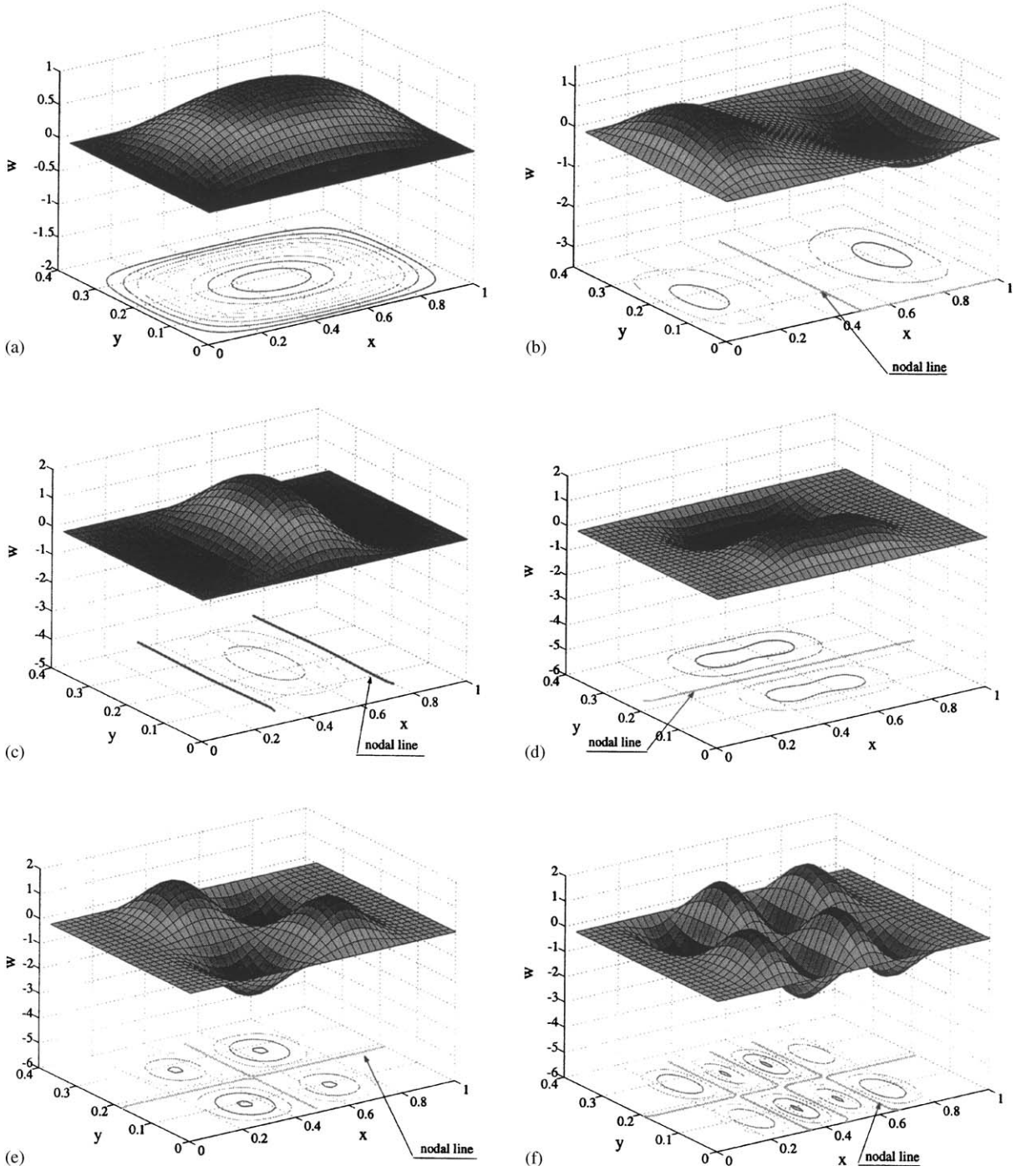

Fig. 7. Vibration mode shapes at different sampling temperatures marked correspondingly in Fig. 6(b): (a) $\delta T/\delta T_{cr} = 3.648 \times 10^{-3}$; (b) $\delta T/\delta T_{cr} = 3.373$; (c) $\delta T/\delta T_{cr} = 7.933$; (d) $\delta T/\delta T_{cr} = 23.258$; (e) $\delta T/\delta T_{cr} = 34.751$; (f) $\delta T/\delta T_{cr} = 42.321$.

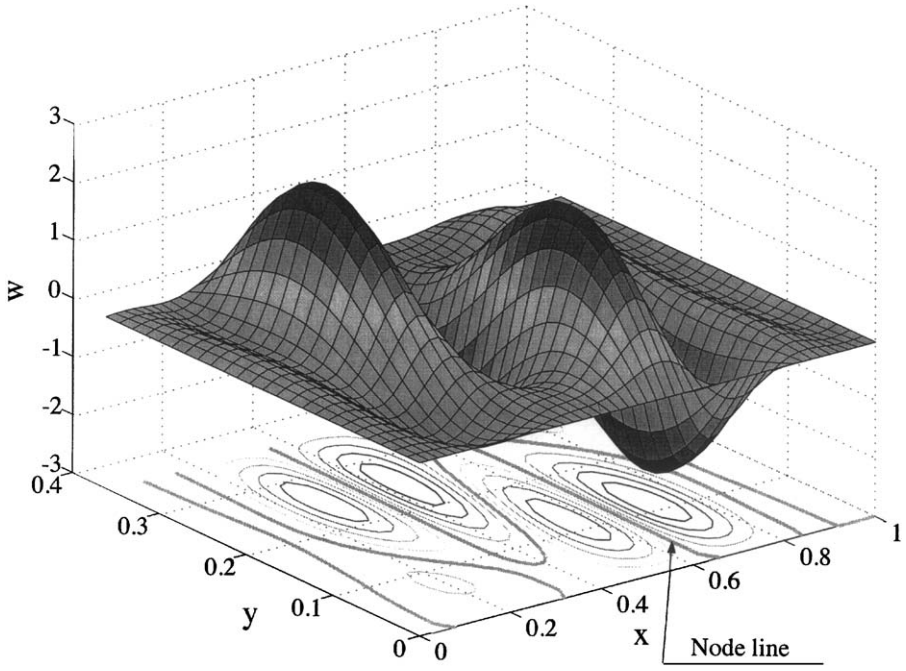

Fig. 8. Vibration mode shape after mode jumping, point (g) marked in Fig. 6(b). $\delta T/\delta T_{cr} = 47.5202$, $A_{61} = -1$, $A_{32} = -0.85424$, $A_{81} = -0.73779$, $A_{52} = -0.64559$, $A_{21} = -0.37279$, $A_{41} = -0.2520$, $A_{92} = -0.17519$, $A_{43} = -0.081812$.

coexistence of three stable equilibria (from 50°C to 69.3°C), see Fig. 3; (2) slow rate of temperature increase enables the system to accumulate the kinetic energy caused by the small perturbations during numerical computation; (3) effect of nearby bifurcation points (see also Fig. 3). With moderate heating rate, the snapping phenomenon can be captured. However, this jumping to the far field stable branch is not unique. It depends on the rate of heating as illustrated in Figs. 9(b) and (c). This kind of indeterminacy has been observed in other dynamical systems [32].

Finite element analysis is also performed to study the snapping phenomenon dynamically. In this procedure, the ascending transient integration is performed after a quasi-static analysis which stops at $\Delta T = 50°C$ (about 80% of the secondary critical value). During the ascending transient stage, the temperature rises from 50°C to 80°C and the moderate heating rate $R = 10°C/s$ as mentioned above is used. The temperature is then reduced to 40°C with the same descending rate. Fig. 10 illustrates hysteretic behavior conducted by the plate. It can be clearly observed from this figure that as the temperature reaches the critical value (67°C) of the primary post-buckling branch, there is a loss of stability and a dynamic jump occurs, resulting in a transient response which oscillates around the new stable branch (finally coming to rest due to the presence of a small amount of damping). Due to the dissipation of the kinetic energy, the trajectory follows this new (stable) equilibrium path just as in the quasi-static case. The most interesting phenomenon happens during the descending stage: after an intermediate jump which occurs at 50°C (corresponding to the bifurcation temperature at which the two target branches lose their stability

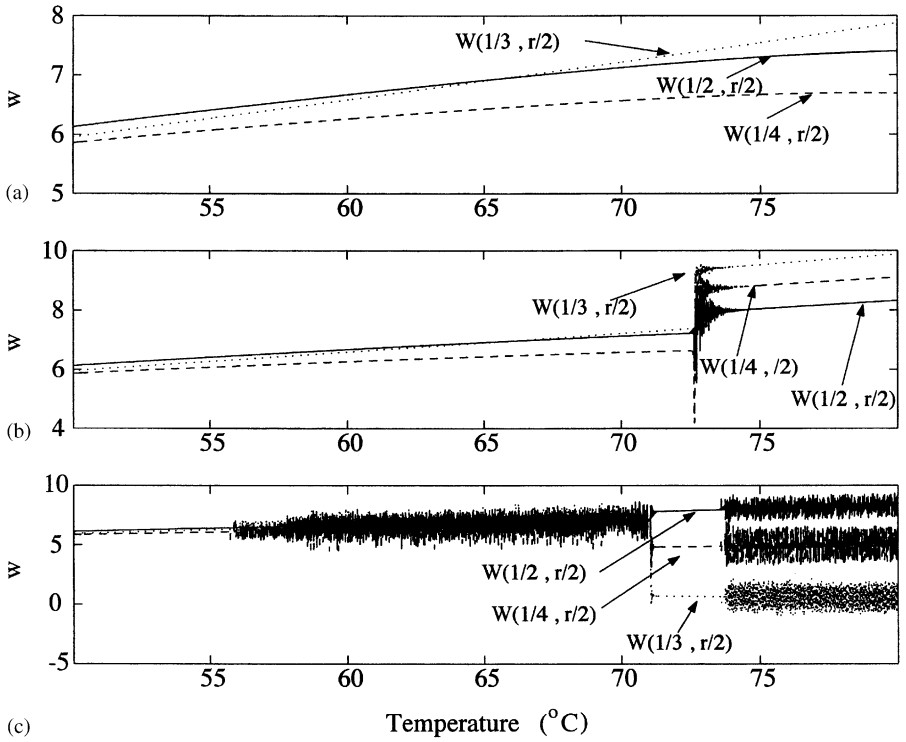

Fig. 9. Transient response of monitored points on the plate during temperature sweeps, analytical approach: (a) fast heating rate ($\Delta T/\Delta t = 100^\circ$C/s); (b) moderate heating rate ($\Delta T/\Delta t = 10^\circ$C/s); (c) slow heating rate ($\Delta T/\Delta t = 1^\circ$C/s).

in Fig. 3), the plate jumps back to its original path when the temperature is reduced to 47°C. In contrast to the analytical approach, the effect of delay caused by the sweeping of the temperature is small. This might be due to the introduction of structural damping in the finite element approach.

5. Concluding remarks

This paper follows a systematic investigation of the various static and dynamic characteristics of modal shifting and mode jumping phenomena exhibited by a thermally loaded, simply-supported, in-plane-fixed plate, using both analytical and finite element approaches. A compact form of the formulation is developed to reduce the PDEs to a system of ODEs in the analytical approach. By this, we can study the effects of arbitrary combinations of the assumed modal components on the secondary bifurcation of the plate.

The lack of compound points found in the linear buckling analysis of the plate with different aspect ratios (demonstrated by the separation of the lowest two critical loads shown in Fig. 2) indicates that the snapping of the post-buckled plate caused by the secondary instability of the equilibrium can only be captured by considering the coupling effects of a large number of assumed

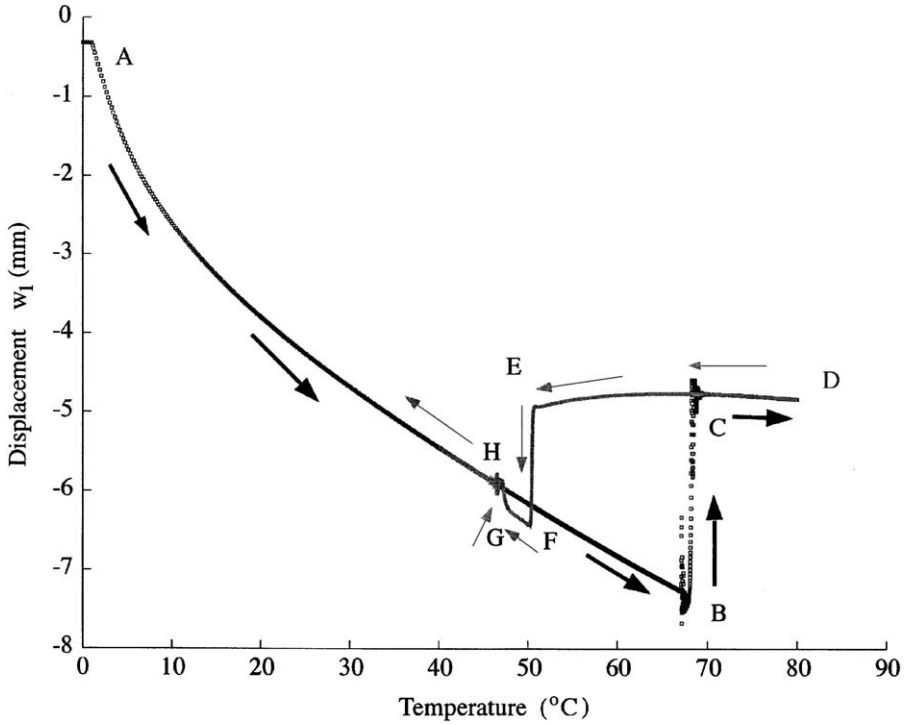

Fig. 10. Transient response of a specific point on the plate using moderate temperature sweep ($\Delta T/\Delta t = 10°\mathrm{C/s}$), finite element approach. Deformation at $(x, y) = (0.3a, 0.5b)$.

modes. Without enough modes, the prediction may be even qualitatively incorrect. This can be attributed to the strong non-linearity introduced by the in-plane constraints, which makes the post-buckling behavior of the plate significantly different from that of an axially (mechanically) compressed plate.

The change of natural frequencies with respect to temperature reflects the dynamic instability characteristics of the plate and can be used to predict the onset of the snapping. A word of caution is necessary, however. The jumping to the farfield stable states is not unique. By this, we mean that for different initial conditions, a different choice of damping, or different ascending or descending sweep rate, other stable post-buckling states may be reached. This is one of the major differences between a linear and a non-linear system. In transient analysis, the dynamic response can be affected by the coexistence of stable equilibriums, the nearby bifurcation points, and the rate of heating.

Modal shifting phenomenon, demonstrated by the exchange of vibration modal shapes at some particular points in the plot of temperature versus natural frequencies, does not occur in the post-secondary buckling regime. As it is well known that bifurcation points usually indicate the breaking of symmetry, our results suggest that while the primary critical point represents the onset of out-of-plane deflection, the secondary critical point initiates the breaking of the symmetry of the post-buckled shapes: on the primary post-buckling path the static deflection is symmetric to both x- and y-axis, while on the target branches (for the mode jumping) the deflection is found to

be antisymmetric to both the x- and y-axis. There is breaking of symmetry of the vibrational modes on these stable equilibrium paths.

When subjected to a non-stationary loading history, represented by the combination of the increasing and decreasing of the loading, slender structures (especially plates) may exhibit a hysteretic behavior. In certain cases this may be modified by an additional buckling phenomenon where the plate response suddenly jumps to another buckled shape. Modelling and characterizing this behavior (including the important dynamic effects) has been achieved using a hybrid static–dynamic finite element approach.

Acknowledgements

The authors acknowledge the assistance of Dr. Kevin Murphy of the University of Connecticut for helpful discussions over the Galerkin approach for thermal loading.

References

[1] M. Stein, Loads and deformations of buckled rectangular plates, NASA Technical Report R-40, National Aeronautics and Space Administration, 1959.

[2] W.J. Supple, On the change in buckle pattern in elastic structures, *International Journal of Mechanical Sciences* 10 (1968) 737–745.

[3] P.R. Everall, G.W. Hunt, Arnold tongue predictions of secondary buckling in thin elastic plates, *Journal of the Mechanics and Physics of Solids* 47 (1999) 2187–2206.

[4] P.R. Everall, G.W. Hunt, Quasi-periodic buckling of an elastic structure under the influence of changing boundary conditions, *Proceedings of the Royal Society of London, Series A* 455 (1999) 3041–3051.

[5] D.G. Schaeffer, M. Golubitsky, Boundary conditions and mode jumping in the buckling of rectangular plate, *Communications in Mathematical Physics* 69 (1979) 209–236.

[6] T. Nakamura, K. Uetani, The secondary buckling and post-secondary-buckling behaviors of rectangular plates, *International Journal of Mechanical Science* 21 (1979) 265–286.

[7] M. Uemura, O. Byon, Secondary buckling of a flat plate under uniaxial compression—part 1: theoretical analysis of simply supported flat plate, *International Journal of Non-Linear Mechanics* 12 (1977) 355–370.

[8] R. Maaskant, J. Roorda, Mode jumping in biaxially compressed plates, *International Journal of Solids and Structures* 29 (1992) 1209–1219.

[9] F. Stoll, Analysis of the snap phenomenon in buckled plates, *International Journal of Non-Linear Mechanics* 29 (1994) 123–138.

[10] E. Riks, C.C. Rankin, F.A. Brogan, On the solution of mode jumping phenomena in thin-walled shell structures, *Computer Methods in Applied Mechanics and Engineering* 136 (1996) 59–92.

[11] E. Riks, C.C. Rankin, Sandwich modeling with an application to the residual strength analysis of a damaged compression panel, *International Journal of Non-Linear Mechanics* 37 (2002) 897–908.

[12] F. Stoll, S.E. Olson, Finite element investigation of the snap phenomenon in buckled plates, in: *Proceedings of the 1997 38th AIAA/ASME/ASCE/AHS/ASC Structures, Structural Dynamics, and Materials Conference*, Vol. 4, 1997, pp. 2703–2712.

[13] H.-Y. Lai, C.-K. Chen, Y.-L. Yeh, Double-mode modeling of chaotic and bifurcation dynamics for a simply supported rectangular plate in large deflection, *International Journal of Non-Linear Mechanics* 37 (2002) 331–343.

[14] N. Tiwari, M.W. Hyer, Secondary buckling of compression-loaded composite plates, *American Institute of Aeronautics and Astronautics Journal* 40 (2002) 2120–2126.

[15] H. Troger, A. Steindl, *Non-linear Stability and Bifurcation Theory—An Introduction to Engineers and Applied Scientists*, Springer, Vienna, 1991.

[16] D.M. Lee, I. Lee, Vibration behaviors of thermally postbuckled anisotropic plates using first-order shear deformable plate theory, *Computers and Structures* 63 (1997) 371–378.
[17] C.S. Chien, S.Y. Gong, Z. Mei, Mode jumping in the von karman equations, *SIAM Journal of Scientific Computing* 22 (2000) 1354–1385.
[18] C.S. Chien, S.L. Shang, Z. Mei, Tracing the buckling of a rectangular plate with the block GMRES method, *Journal of Computational and Applied Mathematics* 136 (2001) 199–218.
[19] B.G. Falzon, D. Hitchings, Capturing mode-switching in postbuckling composite panels using a modified explicit procedure, *Composite Structures* 60 (2003) 447–453.
[20] L.S. Ma, T.J. Wang, Thermal postbuckling and bending behavior of circular plates with temperature dependent material properties, *Key Engineering Materials* 243–244 (2003) 195–200.
[21] P.R. Everall, G.W. Hunt, Mode jumping in the buckling of struts and plates: a comparative study, *International Journal of Non-Linear Mechanics* 35 (2000) 1067–1079.
[22] S. Ilanko, Vibration and post-buckling of in-plane loaded rectangular plates using a multiterm galerkin's method, *Journal of Applied Mechanics* 69 (2002) 589–592.
[23] K.D. Murphy, D. Ferreira, Thermal buckling of rectangular plates, *International Journal of Solids and Structures* 38 (2001) 3979–3994.
[24] H.S. Shen, Thermomechanical post-buckling analysis of imperfect laminated plates using a higher-order shear-deformation theory, *Computers and Structures* 66 (1998) 395–409.
[25] G.W. Hunt, P.R. Everall, Arnold tongues and mode-jumping in the supercritical post-buckling of an archetypal elastic structure, *Proceedings of the Royal Society of London, Series A* 445 (1999) 125–140.
[26] L.N. Virgin, H. Chen, The dynamics of mode jumping in thermally buckled plates, in: *Eighth International Conference on Recent Advances in Structural Dynamics*, Southampton, UK, July 2003.
[27] J. Marcinowski, Postbuckling behaviour of rectangular plates in axial compression, *Archives of Civil Engineering* 45 (1999) 275–288.
[28] E.J. Doedel, A.R. Champneys, T.F. Fairgrieve, Y.A. Kuznetsov, B. Sandstede, X.-J. Wang, AUTO97: continuation and bifurcation software for ordinary differential equations, Technical Report, Department of Computer Science, Concordia University, Montreal, Canada, 1997, available by FTP from ftp.cs.concordia.ca in directory pub/doedel/auto.
[29] E.H. Dowell, *Aeroelasticity of Plates and Shells*, Noordhoff International Publishing, Leyden, The Netherlands, 1975.
[30] L.N. Virgin, R.H. Plaut, Use of frequency data to predict secondary bifurcation, *Journal of Sound and Vibration* 251 (2002) 919–926.
[31] A.W. Leissa, Vibration of plates, NASA Technical Report SP-160, National Aeronautics and Space Administration, 1969.
[32] J.M.T. Thompson, H.B. Stewart, *Nonlinear Dynamics and Chaos*, 2nd Edition, Wiley, New York, 2002.